JOURNAL OF GUIDANCE, CONTROL, AND DYNAMICS
Vol. 32, No. 5, September–October 2009

Stability of Sun-Synchronous Orbits in the Vicinity of a Comet

Sharyl M. Byram*
University of Michigan, Ann Arbor, Michigan 48109
and
Daniel J. Scheeres†
University of Colorado, Boulder, Colorado 80309

DOI: 10.2514/1.41655

This paper identifies and analyzes stable sun-synchronous orbits in a Hill rotating frame that can be applied to any small body in the solar system. The stability of these orbits is due to the inclusion of solar radiation pressure effects. The stability of the orbits from escaping the comet are analyzed using the construction of zero-velocity curves for the system considered as well as spectral analysis. The stability analysis also considers the effect of orbital perturbations from outgassing jets on a spacecraft in orbit about a comet. Once these orbits have been identified, impulsive control schemes to restrict a stable orbit's motion are explored, showing that it is feasible to implement a form of orbital hovering in the terminator plane of a comet.

I. Introduction

THE recent rise in missions to small bodies has created a new set of dynamical problems to be solved. Although many missions have flown by and investigated comets from a distance, there has yet to be a mission to actually orbit and land on the surface of one. This need to safely orbit a comet has become important as NASA has recently stressed the importance of obtaining a comet surface sample return[‡], and ESA's Rosetta mission is scheduled to deliver a lander to the surface of comet 67 P/Churyumov–Gerasimenko in 2014. These types of missions will involve a period of close proximity to the comet and potentially an orbital phase about the body. Therefore, our focus will be to identify and analyze stable sun-synchronous orbits in a rotating frame. Note that we define stability as the spacecraft not escaping from the comet, that is, by being bounded in the vicinity of a comet without impacting. Although the orbits explored can be used to orbit any small body in the solar system, particular attention to the case of comets with outgassing jets is considered.

Previous work has been done on this problem. Dankowicz [1] found a class of orbits offset from an asteroid in a nonrotating system and explored their stability. Scheeres and Marzari [2] investigated the stability of such motions accounting for the orbit of the comet and the gravitational attraction of the sun. Scheeres [3] investigated the definition and stability of sun-synchronous orbits started from the terminator plane, but did not incorporate an orbit offset for these. The current research combines the offset orbits of Dankowicz [1] with the averaging analysis and rotation present in the Scheeres analysis. The stability of the identified orbits will be tested for outgassing jet accelerations in the case of comets. Once these orbits have been shown to be stable, different control schemes to restrict their allowable motion will be explored, creating a new class of "hovering" orbits at a comet. Restricted orbits are useful for mapping the comet's surface or monitoring the surface activity at the sunrise or sunset terminator.

Presented as Paper 7202 at the Astrodynamic Specialists, Honolulu, HI; received 16 October 2008; revision received 17 February 2009; accepted for publication 19 February 2009.

*Ph.D. Candidate, Department of Aerospace Engineering; byramsm@umich.edu.

†A. Richard Seebass Chair, Professor, Department of Aerospace Engineering Sciences; scheeres@colorado.edu.

II. Equations of Motion

Consider the general case of a spacecraft in the vicinity of a comet and significantly far from any other celestial body. The spacecraft is considered to have negligible mass relative to the comet, which is modeled as a point mass and is subject to solar radiation pressure acting in the antisunward direction, $\hat{d}$. In an inertial frame, the equations of motion for the spacecraft are

$$\ddot{\mathbf{r}}_I = (\partial U/\partial \mathbf{r}_I) + g\hat{d} \tag{1}$$

where $\mathbf{r}_I$ is the position vector in an inertial frame, U is the comet's gravitational potential, and g is the solar radiation pressure magnitude computed as

$$g = \beta/d^2 \tag{2}$$

where $\beta = (1+\eta)G_1/B$, $G_1 = 1\times 10^8$ kg $\cdot$ km^3/(s$^2\cdot$ m^2), B is the spacecraft mass-to-area ratio in kilograms per meter squared, η is the reflectance of the spacecraft, and d is the heliocentric distance of the comet in kilometers [3]. The Hill equations of motion are appropriate to use in this case given the dynamical setup. They are as follows in the comet orbit frame assuming a constant rotation about the sun (with x along the sun–comet line and z out of the orbital plane):

$$\ddot{x} = 2\omega\dot{y} + 3\omega^2 x - (\mu x/r^3) + g \tag{3}$$

$$\ddot{y} = -2\omega\dot{x} - (\mu y/r^3) \tag{4}$$

$$\ddot{z} = -\omega^2 z - (\mu z/r^3) \tag{5}$$

where $r = \sqrt{x^2+y^2+z^2}$. The Hill equations of motion in Cartesian coordinates have a Jacobi integral of [6]

$$J = \tfrac{1}{2}(\dot{x}^2+\dot{y}^2+\dot{z}^2) - (\mu/r) - \tfrac{1}{2}\omega^2(3x^2-z^2) - gx \tag{6}$$

Note that for a constant rotation rate, ω, this integral is conserved. Although cometary orbits do not generally have a constant angular rate, over the short time spans considered in this paper, a constant rate is a good approximation to the true system. A cylindrical frame, illustrated in Fig. 1, will gain us more insight; therefore, we apply the following transformation:

[‡]Announcement of Opportunity: New Frontiers Program 2003 and Missions of Opportunity (AO-03-OSS-03), NASA, October 2003, http://research.hq.nasa.gov/code s/nra/current/AO-03-OSS-03/index.html [retrieved November 2007]

$$x = x \tag{7}$$

$$y = \rho\cos\theta \tag{8}$$

$$z = \rho\sin\theta \tag{9}$$

$$\dot{x} = \dot{x} \tag{10}$$

$$\dot{y} = \dot{\rho}\cos\theta - \rho\dot{\theta}\sin\theta \tag{11}$$

$$\dot{z} = \dot{\rho}\sin\theta + \rho\dot{\theta}\cos\theta \tag{12}$$

Converting to the cylindrical coordinates, the equations of motion become

$$\ddot{x} = 2\omega(\dot{\rho}\cos\theta - \rho\dot{\theta}\sin\theta) + 3\omega^2 x + g - (x\mu/r^3) \tag{13}$$

$$\ddot{\rho} = -2\dot{x}\omega\cos\theta + \rho\dot{\theta}^2 - \rho\omega^2\sin^2\theta - (\rho\mu/r^3) \tag{14}$$

$$\rho\ddot{\theta} = 2\dot{x}\omega\sin\theta - 2\dot{\rho}\,\dot{\theta} - \rho\omega^2\sin\theta\cos\theta \tag{15}$$

where $r = \sqrt{x^2 + \rho^2}$. Note that a symmetry in the evolution of the x and ρ states exists for $+\dot{\theta}$ and $-\dot{\theta}$ when $\theta_0 = 0, \pi$. This is expected due to the term $\dot{\theta}\sin\theta = -\dot{\theta}\sin(-\theta)$ in the $\ddot{x}$ equation and $\dot{\theta}^2 = (-\dot{\theta})^2$ in the $\ddot{\rho}$ equation. For completeness, the Hill equations of motion in cylindrical coordinates have a Jacobi integral of

$$J = \tfrac{1}{2}(\dot{x}^2 + \dot{\rho}^2 + \rho^2\dot{\theta}^2) - (\mu/r) - \tfrac{1}{2}\omega^2(3x^2 - \rho^2\sin(\theta)^2) - gx \tag{16}$$

A. Nonrotating Equilibrium Solution

The system studied by Dankowicz [1] is a nonrotating two-body problem with the addition of solar radiation pressure to the secondary body. The equations of motion used (in cylindrical coordinates) are as follows:

$$\ddot{x} = -(\mu x/r^3) + g \tag{17}$$

$$\ddot{\rho} = \rho\dot{\theta}^2 - (\mu\rho/r^3) \tag{18}$$

$$\rho\ddot{\theta} = -2\dot{\rho}\,\dot{\theta}/\rho \tag{19}$$

Note that these are the same equations of motion described earlier if ω is set to 0. Directly integrating Eq. (19) leads to $\rho^2\dot{\theta} = h$, which is a constant angular momentum about the sun–comet line. Dankowicz [1] found relative equilibrium solutions to these equations as a class of circular orbits with the following conditions:

$$0 = (\mu/r^3) - (g/x) \tag{20}$$

$$0 = (h^2/\rho^4) - (g/x) \tag{21}$$

This nonrotating system's equilibrium solutions will be the basis for the exploration of averaging the Hill equations of motion. These solutions produce a family of sun-synchronous circular orbits perpendicular to the sun–comet line. The orbits that are closest to the body are stable and, as the x offset gets larger, the orbits become unstable with equilibrium solutions not existing for all values of x. At a given equilibrium, x_0 and ρ_0, the angle varies as $\theta = \theta_0 + h/\rho_0^2 * t$.

B. Averaging Procedure

If we assume that the rotation rate, ω, is small, then we can derive a set of equations incorporating the rotational terms and eliminating the time-varying θ term. If we assume the nominal motion is along the circular orbit found for the nonrotating system, the equations of motion for the rotating system can be rewritten as

$$\dot{\mathbf{x}} = f(x, \rho, \dot{x}, \dot{\rho}, \dot{\theta}) + \omega^2 g(x, \rho, \theta, \dot{x}, \dot{\rho}, \dot{\theta}) \tag{22}$$

where $\mathbf{x}$ is the state vector of the system, $f(x, \rho, \dot{x}, \dot{\rho}, \dot{\theta})$ are the nonrotating terms of the equations of motion, and $\omega^2 g(x, \rho, \theta, \dot{x}, \dot{\rho}, \dot{\theta})$ are the rotational terms. Note that only the $g(x, \rho, \theta, \dot{x}, \dot{\rho}, \dot{\theta})$ terms are a function of t through θ. Then we introduce an averaging operator to extract the effect of the $g(x, \rho, \theta, \dot{x}, \dot{\rho}, \dot{\theta})$ function over one orbit.

Let us consider a generic function, $h(\theta)$, which is a function of the cylindrical coordinate θ. If this function is averaged over a full rotation through the θ variable, then the averaging procedure is of the following form:

$$\bar{h} = \frac{1}{2\pi}\int_0^{2\pi} h(\theta)\,\mathrm{d}\theta \tag{23}$$

If Eqs. (13–15) are averaged over θ in this way, a system similar to the two-body nonrotating system from Dankowicz [1] is recovered with the additional terms of $3\omega^2\bar{x}$ and $-\frac{1}{2}\bar{\rho}\omega^2$.

$$\ddot{\bar{x}} = g - (\bar{x}\mu/r^3) + 3\omega^2\bar{x} \tag{24}$$

$$\ddot{\bar{\rho}} = \bar{\rho}\dot{\bar{\theta}}^2 - \tfrac{1}{2}\bar{\rho}\omega^2 - (\bar{\rho}\mu/r^3) \tag{25}$$

$$\bar{\rho}\,\ddot{\bar{\theta}} = -2\dot{\bar{\rho}}\,\dot{\bar{\theta}} \tag{26}$$

where $\bar{r} = \sqrt{\bar{x}^2 + \bar{\rho}^2}$. Note that Eq. (26) can be directly integrated as follows:

$$\bar{\rho}^2\dot{\bar{\theta}} = h \tag{27}$$

where h is a constant and, in this case, is the averaged angular momentum magnitude. Therefore, the averaged equations of motion reduce to functions of $\bar{x}$ and $\bar{\rho}$ with constant h:

$$\ddot{\bar{x}} = g - (\bar{x}\mu/\bar{r}^3) + 3\omega^2\bar{x} \tag{28}$$

$$\ddot{\bar{\rho}} = \bar{\rho}[(h^2/\bar{\rho}^4) - \tfrac{1}{2}\omega^2 - (\mu/\bar{r}^3)] \tag{29}$$

with an averaged Jacobi integral of

$$\bar{J} = \tfrac{1}{2}(\dot{\bar{x}}^2 + \dot{\bar{\rho}}^2) - (\mu/r) - \tfrac{1}{2}\omega^2(3\bar{x}^2 - \tfrac{1}{2}\bar{\rho}^2) - g\bar{x} + (h^2/2\bar{\rho}^2) \tag{30}$$

where $\dot{\bar{\theta}} = h/\bar{\rho}^2$. Note that this same Jacobi integral can be obtained by examining the averaged equations alone, where $V = (\mu/r) + \frac{1}{2}\omega^2(3\bar{x}^2 - \frac{1}{2}\bar{\rho}^2) + g\bar{x} - (h^2/2\bar{\rho}^2)$. Dankowicz [1] discovered that the angular momentum projected along the sun–comet line was constant for the nonrotating system. The angular momentum projected along the solar radiation direction, $\hat{x}$, for this rotating frame system is

$$h_d = \hat{x}\cdot(\mathbf{r}\times\dot{\mathbf{r}}) \tag{31}$$

where its projected time derivative has the following form:

$$\dot{h}_d = \hat{x}\cdot(\mathbf{r}\times\ddot{\mathbf{r}}) \tag{32}$$

If $\mathbf{r} = (x, y, z)$ and $\dot{\mathbf{r}} = (\dot{x}, \dot{y}, \dot{z})$, then this time derivative simply reduces to

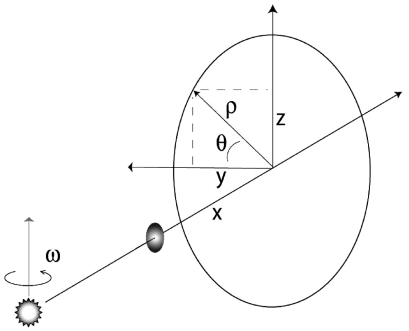

Fig. 1 Relative Hill coordinate frames: Cartesian and cylindrical.

$$\dot{h_d} = \hat{x} \cdot (2\omega\dot{x}z - \omega^2 yz, gz + 2\omega\dot{y}z + 4\omega^2 xz, -gy - 2\omega(x\dot{x} + y\dot{y}) - 3\omega^2 xy) \tag{33}$$

$$\dot{h_d} = 2\omega\dot{x}z - \omega^2 yz \tag{34}$$

Changing the variables to cylindrical coordinates results in an angular momentum derivative of

$$\dot{h_d} = 2\omega\dot{x}\rho\sin\theta - \tfrac{1}{2}\omega^2\rho^2\sin(2\theta) \tag{35}$$

Applying the averaging procedure, Eq. (23), to the projected angular momentum derivative shows that the average value of $\dot{h_d}$ over 2π in θ is 0 due to the $\sin\theta$ and $\sin(2\theta)$ terms if we assume constant values for ρ and ω and a zero or periodic value for $\dot{x}$. This means that the projected angular momentum along $\hat{x}_s$ is conserved, on average, when orbiting along one of the offset terminator orbits. This conservation of the projected angular momentum implies that, on average, the dynamics in this rotating system have similarities to the nonrotating system found in Dankowicz [1].

III. Equilibrium Solutions

To find the equilibrium solutions to this set of equations, we set $\ddot{\bar{x}}$ and $\ddot{\bar{\rho}}$ to 0 and find that the following conditions must hold:

$$3\omega^2 = (\mu/\bar{r}^3) - (g/\bar{x}) \tag{36}$$

$$\tfrac{7}{2}\omega^2 = (h^2/\bar{\rho}^4) - (g/\bar{x}) \tag{37}$$

Note that these conditions are similar to the ones found by Dankowicz [1] with a perturbation from the rotation, ω. For a given value of initial averaged x offset, $\bar{x}_0$, then the variables $\bar{\rho}_0$, $\dot{\bar{\theta}}_0$, and h_0 can be found as functions of $\bar{x}_0$, yielding a family of circular orbits perpendicular to the sun line that are sun synchronous:

$$\bar{\rho}_0 = \sqrt{\left(\frac{\bar{x}_0\mu}{3\omega^2\bar{x}_0 + g}\right)^{2/3} - \bar{x}_0^2} \tag{38}$$

$$\dot{\bar{\theta}}_0 = (7\omega^2/2) + (g/\bar{x}_0) \tag{39}$$

$$h_0 = \bar{\rho}_0^2\dot{\bar{\theta}}_0 \tag{40}$$

Note that these solutions are dependent on the values of μ, ω, and g, resulting in different family profiles for each system. Again, these solutions do not exist for all x_0. An example profile of the family of circular orbits with a 0.25 km diameter body with a 200 kg/m^3 bulk density at approximately 3 astronomical units, yielding values of $\mu = 1.1972e-10$ km^3/s^2, $\omega = 3.7749e-8$ rad/s, and $g = 1.4749e-11$ km/s^2, can be seen in Fig. 2, whereas Figs. 3–6 illustrate trajectory examples in the vicinity of these circular orbits. Note that the larger the x offset, the more the trajectory deviates from the averaged solution. The stability as a function of the x_0 offsets is discussed in Sec. V. These orbits can be considered generalizations of the terminator orbits described in Scheeres [3]. It is important to note that these orbits are sun-synchronous and will ideally always present the same orientation to the sun.

IV. Zero-Velocity Curves

It is instructive to construct the zero-velocity curves that exist for this problem to gain insight into the dynamics of the system. These curves will also help determine if there are any trajectories that may be trapped. To find the zero-velocity curves, we set the averaged Jacobi integral, Eq. (30), to some arbitrary constant, C, and the velocities to 0.

$$C = -(\mu/\bar{r}) - \tfrac{1}{2}\omega^2\left(3\bar{x}^2 - \tfrac{1}{2}\bar{\rho}^2\right) - g\bar{x} + (h^2/2\bar{\rho}^2) \tag{41}$$

Note that $C = -V$ as expected; therefore, for a given value of C, the spacecraft's motion can occur where

$$C + V \geq 0 \tag{42}$$

To find the zero-velocity curves, we consider the following simplified equation:

$$C_m + (\mu/\bar{r}) + \tfrac{1}{4}\omega^2\bar{\rho}^2 - (h^2/2\bar{\rho}^2) = 0 \tag{43}$$

where

$$C_m = C + \tfrac{3}{2}\omega^2\bar{x}^2 + g\bar{x} \tag{44}$$

C_m is considered a constant for a given value of $\bar{x}$. Rearranging Eq. (43), the zero-velocity curves can be found by solving for the roots of the following polynomial:

$$\begin{aligned} 0 = {} & (\tfrac{1}{16}\omega^4)\bar{\Gamma}^5 + (-\tfrac{1}{2}C_m\omega^2 + \tfrac{1}{16}\omega^4\bar{x}^2)\bar{\Gamma}^4 \\ & + (C_m^2 + \tfrac{1}{4}h^2\omega^2 - \tfrac{1}{2}C_m\omega^2\bar{x}^2)\bar{\Gamma}^3 \\ & + (-\mu^2 - C_m h^2 + C_m^2\bar{x}^2 + \tfrac{1}{4}h^2\omega^2\bar{x}^2)\bar{\Gamma}^2 \\ & + (\tfrac{1}{4}h^4 - C_m h^2\bar{x}^2)\bar{\Gamma} + (\tfrac{1}{4}h^4\bar{x}^2) \end{aligned} \tag{45}$$

Note that only values of $\bar{\rho} \geq 0$ are appropriate in cylindrical coordinates, and so the variable $\bar{\Gamma} = \bar{\rho}^2$ is used in the polynomial. For a given, $\bar{x}$, h, C, and g, the zero-velocity curves can therefore be computed. Figure 7 (detailed view in Fig. 8) shows the zero-velocity curves for various circular orbit equilibrium solutions within a family. Note that, as the x offset gets small, the area of allowable

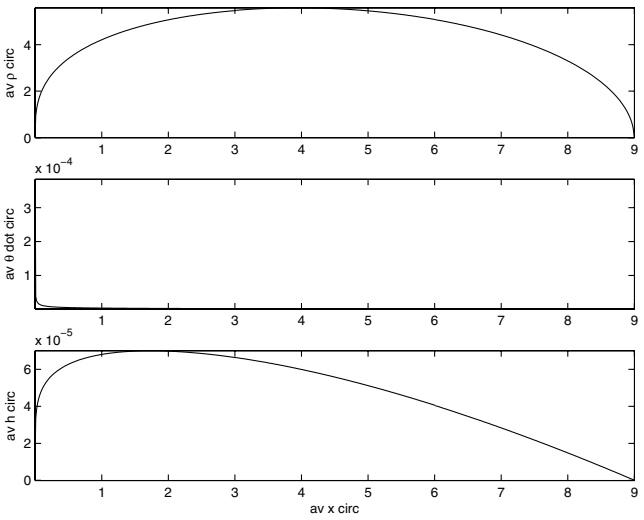

Fig. 2 Example of circular orbit equilibrium solutions of the averaged equations as a function of the x offset.

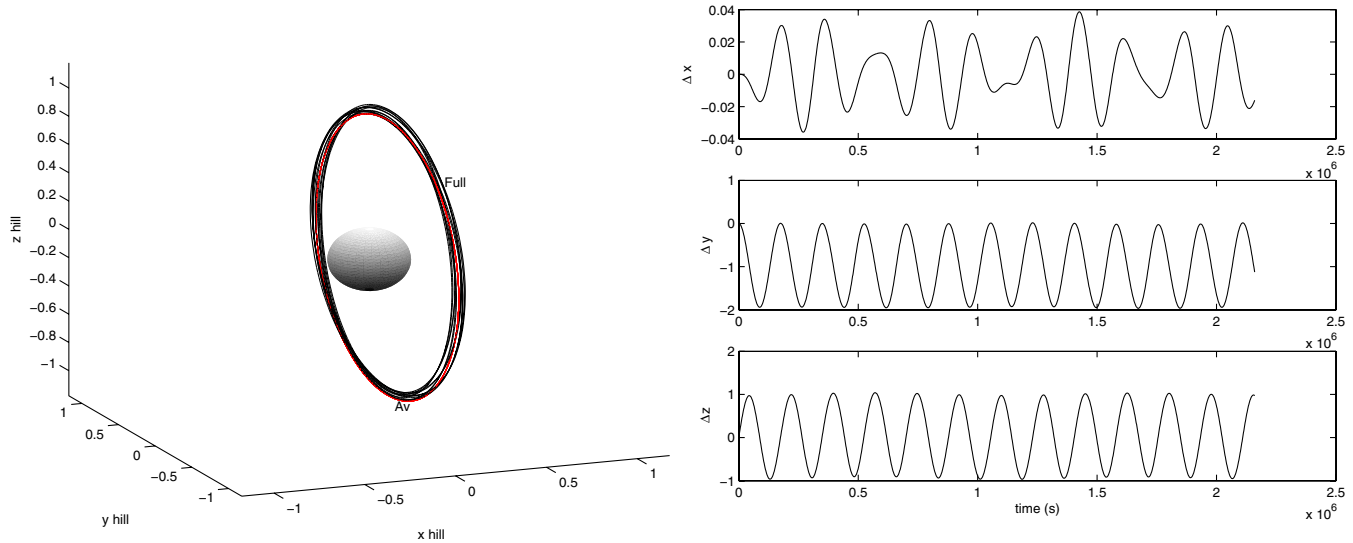

Fig. 3 Initial offset ($x_0 = 0.1$ km) orbit about a comet with a regular gravity field in the rotating frame showing the full and average equations of motion trajectory (shown with full equations' component deviation (Δx, Δy, and Δz) from the averaged solution).

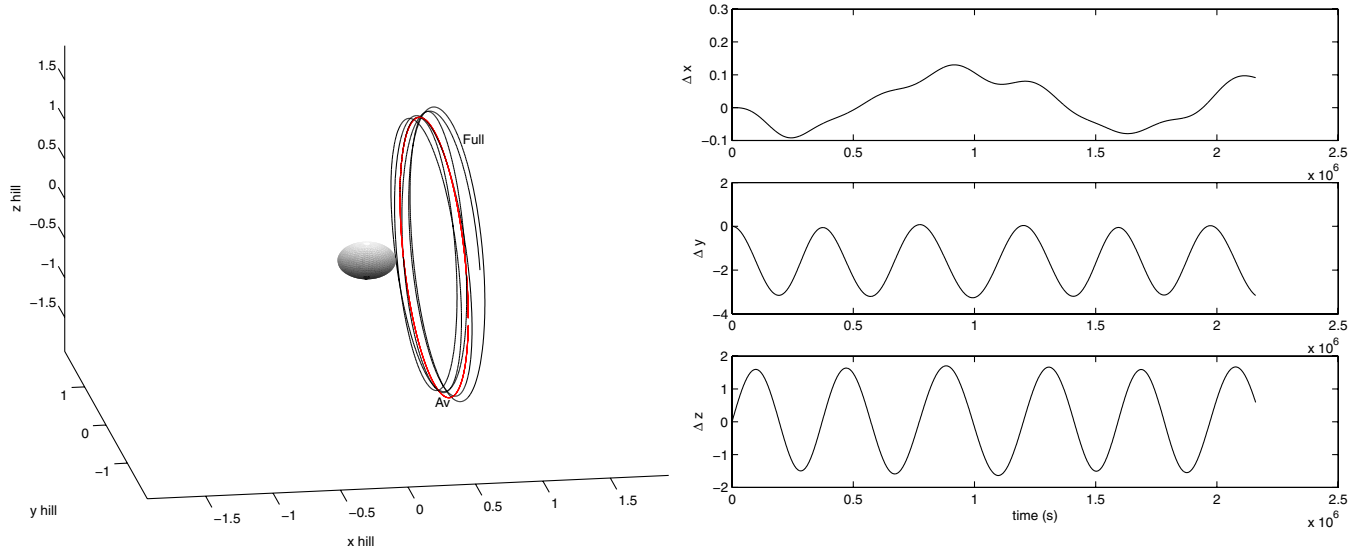

Fig. 4 Initial offset ($x_0 = 0.5$ km) orbit about a comet with a regular gravity field in the rotating frame showing the full and average equations of motion trajectory (shown with full equations' component deviation (Δx, Δy, and Δz) from the averaged solution).

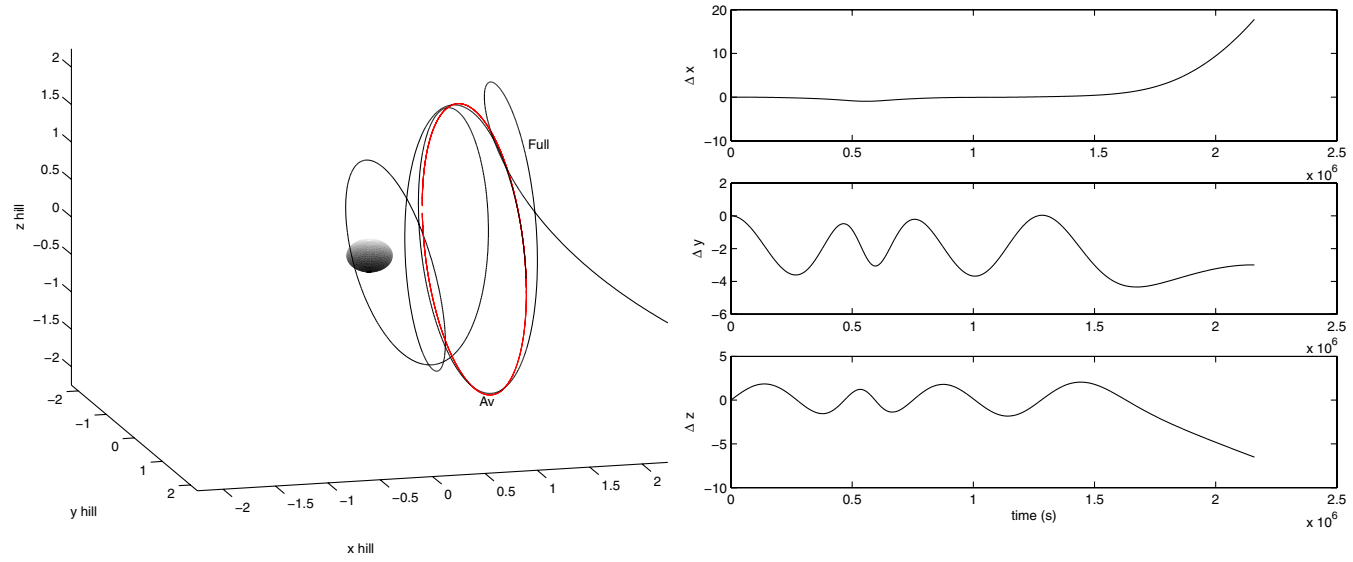

Fig. 5 Initial offset ($x_0 = 1$ km) orbit about a comet with a regular gravity field in the rotating frame showing the full and average equations of motion trajectory (shown with full equations' component deviation (Δx, Δy, and Δz) from the averaged solution).

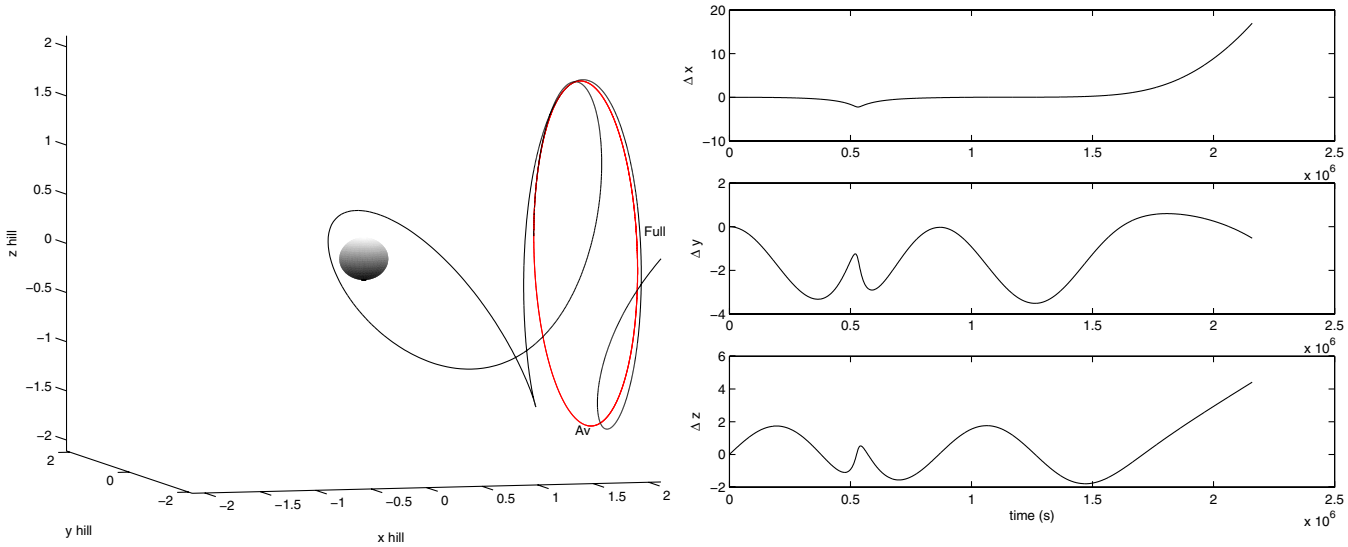

Fig. 6 Initial offset ($x_0 = 2$ km) orbit about a comet with a regular gravity field in the rotating frame showing the full and average equations of motion trajectory (shown with full equations' component deviation (Δx, Δy, and Δz) from the averaged solution).

motion on the sun side of the equilibrium solution reduces until the equilibrium solution becomes a disconnected stable point from the zero-velocity curve. Visually this limit appears to be a stable/unstable boundary for the circular orbit equilibrium solutions, although this will be analytically verified in Sec. V. Figure 9 shows the curves for differing values of C while holding h, ω, and g constant. For an h value associated with a stable equilibrium solution, increasing the energy opens up the allowable area for motion around the equilibrium point and a large-enough value leads to the two areas merging together at a conjugate unstable equilibrium point that has the same h value.

The shape or curvature of the zero-velocity curves is determined by the solar radiation pressure magnitude, g. Larger values of g will tend to straighten the upper portion of the zero-velocity curve and shrink the area of allowable motion for a fixed value of h, as seen in Fig. 10 for a system with constant h and ω and varied solar radiation pressure magnitude.

V. Stability of Averaged Equations of Motion

The zero-velocity curves provide a graphical look at the stability of the system; we now verify these results analytically. To begin, the averaged equations are linearized about a circular orbit equilibrium solution ($\bar{\rho}_0$, $\bar{x}_0$, and $\dot{\bar{\theta}}_0$ from the earlier relations), yielding the following linear equations with time-invariant coefficients:

$$\delta\ddot{\bar{x}} = \left(\frac{3\bar{x}_0^2\mu}{\bar{r}_0^5} - \frac{\mu}{\bar{r}_0^3} + 3\omega^2\right)\delta\bar{x} + \left(\frac{3\bar{x}_0\bar{\rho}_0\mu}{\bar{r}_0^5}\right)\delta\bar{\rho} \tag{46}$$

$$\delta\ddot{\bar{\rho}} = \left(\frac{3\bar{x}_0\bar{\rho}_0\mu}{\bar{r}_0^5}\right)\delta\bar{x} + \left(\frac{3\bar{\rho}_0^2\mu}{\bar{r}_0^5} - \frac{\mu}{\bar{r}_0^3} + \dot{\bar{\theta}}_0^2 - \tfrac{1}{2}\omega^2\right)\delta\bar{\rho} + (2\bar{\rho}_0\dot{\bar{\theta}}_0)\delta\dot{\bar{\theta}} \tag{47}$$

$$\delta\ddot{\bar{\theta}} = \left(\frac{2\dot{\bar{\rho}}_0\dot{\bar{\theta}}_0}{\bar{\rho}_0^2}\right)\delta\bar{\rho} + \left(\frac{-2\dot{\bar{\theta}}_0}{\bar{\rho}_0}\right)\delta\dot{\bar{\rho}} + \left(\frac{-2\dot{\bar{\rho}}_0}{\bar{\rho}_0}\right)\delta\dot{\bar{\theta}} \tag{48}$$

Note that, for a circular orbit, $\dot{\bar{\rho}}_0 = 0$; therefore, Eq. (48) becomes

$$\delta\ddot{\bar{\theta}} = (-2\dot{\bar{\theta}}_0/\bar{\rho}_0^2)\delta\dot{\bar{\rho}} \tag{49}$$

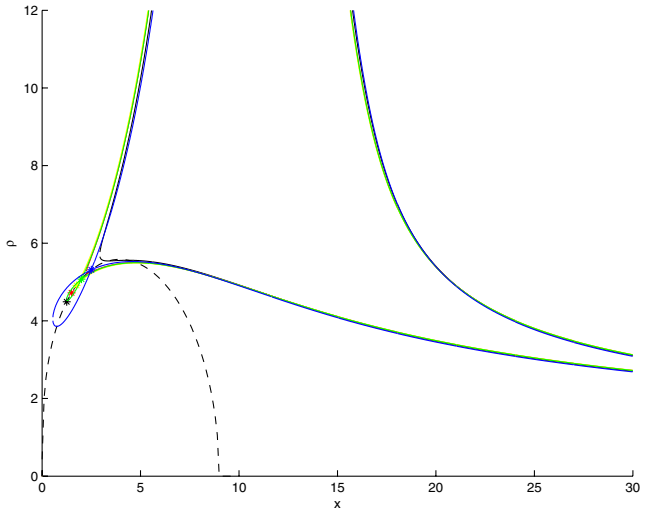

Fig. 7 Zero-velocity curves for various equilibrium solutions. The star refers to the equilibrium solution at each C energy level, the dashed line refers to the circular orbit equilibrium solutions curve, and the solid line refers to the decreasing C curve.

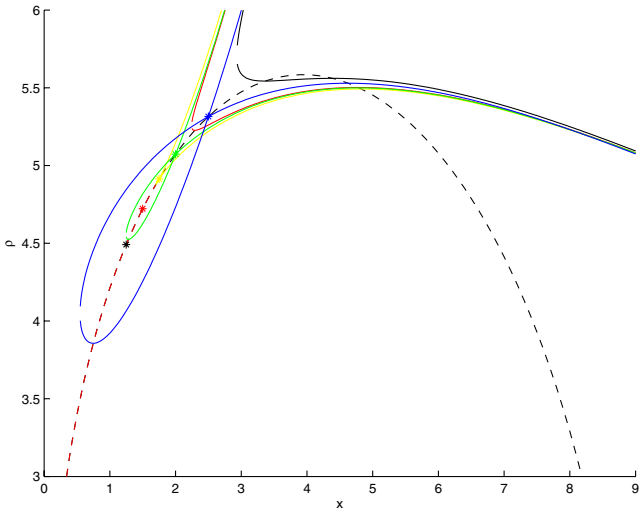

Fig. 8 Zero-velocity curves detail for various equilibrium solutions. The star refers to the equilibrium solution at each C energy level, the dashed line refers to the circular orbit equilibrium solutions curve, and the solid line refers to the decreasing C curve.

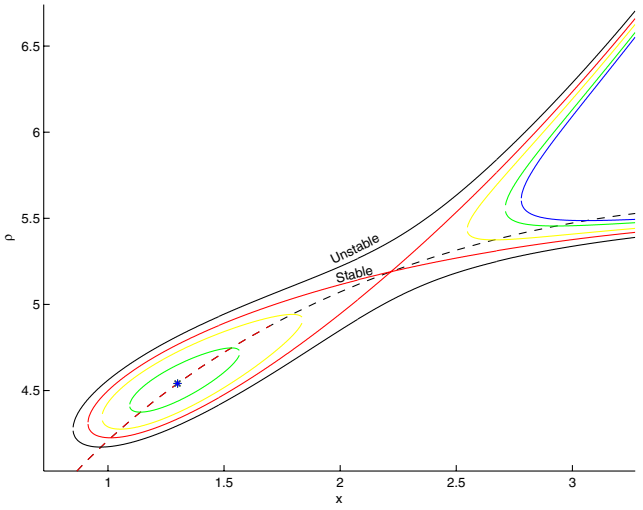

Fig. 9 Zero-velocity curves with constant h. The star refers to the equilibrium solution at each C energy level, the dashed line refers to the circular orbit equilibrium solutions curve, and the solid line refers to the decreasing C curve.

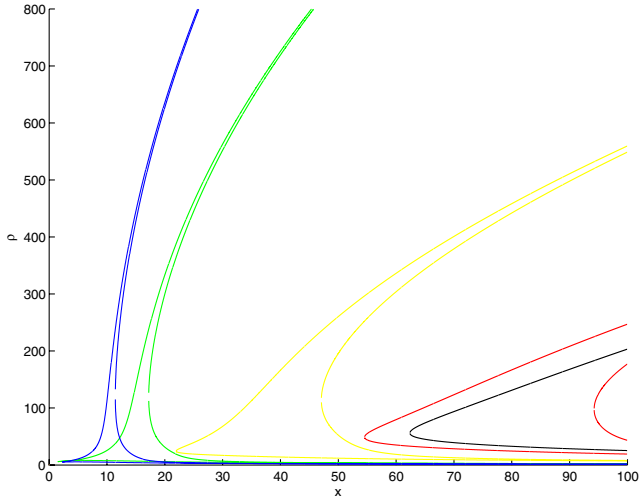

Fig. 10 Zero-velocity curves for fixed ω and varied g. As the g value increases, the curves approach $x = 0$.

For notational simplicity, these equations are rewritten as

$$\delta\ddot{\bar{x}} = a\delta\bar{x} + b\delta\bar{\rho} \tag{50}$$

$$\delta\ddot{\bar{\rho}} = c\delta\bar{x} + d\delta\bar{\rho} + e\delta\dot{\bar{\theta}} \tag{51}$$

$$\delta\ddot{\bar{\theta}} = f\delta\dot{\bar{\rho}} \tag{52}$$

where a, b, c, d, e, and f are defined by the original linearized averaged equations, and $c = b$. In state-space form, the linearized averaged equations are

$$\begin{pmatrix} \delta\dot{\bar{x}} \\ \delta\dot{\bar{\rho}} \\ \delta\dot{\bar{\theta}} \\ \delta\ddot{\bar{x}} \\ \delta\ddot{\bar{\rho}} \\ \delta\ddot{\bar{\theta}} \end{pmatrix} = \begin{pmatrix} 0 & 0 & 0 & 1 & 0 & 0 \\ 0 & 0 & 0 & 0 & 1 & 0 \\ 0 & 0 & 0 & 0 & 0 & 1 \\ a & b & 0 & 0 & 0 & 0 \\ b & d & 0 & 0 & 0 & e \\ 0 & 0 & 0 & 0 & f & 0 \end{pmatrix} \begin{pmatrix} \delta\bar{x} \\ \delta\bar{\rho} \\ \delta\bar{\theta} \\ \delta\dot{\bar{x}} \\ \delta\dot{\bar{\rho}} \\ \delta\dot{\bar{\theta}} \end{pmatrix} \tag{53}$$

$$\dot{\bar{\mathbf{X}}} = \mathbf{A}\bar{\mathbf{X}} \tag{54}$$

To determine the stability of this system, let us examine the eigenvalues of the $\mathbf{A}$ matrix, which are determined by its characteristic polynomial

$$\lambda^6 + (-a - d - ef)\lambda^4 + (-b^2 + ad + aef)\lambda^2 = 0 \tag{55}$$

It is obvious from the characteristic polynomial that there exist two eigenvalues at 0. Therefore, the system is by definition unstable, but the eigenvector associated with the zero eigenvalues is (0,0,1,0,0,0) or the θ direction, which does not affect the stability of the circular orbit but only yields a down track drift. Therefore, it is the other eigenvalues that will be used to determine the stability of the orbit. Eliminating the zero roots of the characteristic polynomial results in

$$\lambda^4 + (-a - d - ef)\lambda^2 + (-b^2 + ad + aef) = 0 \tag{56}$$

which has the roots

$$\lambda = \pm\sqrt{\frac{(a + d + ef) \pm \sqrt{(4b^2 + (-a + d + ef)^2)}}{2}} \tag{57}$$

where

$$(4b^2 + (-a + d + ef)^2) = \frac{36\mu^2\bar{x}_0^2\bar{\rho}_0^2}{(\bar{x}_0^2 + \bar{\rho}_0^2)^5} + \left(3\dot{\bar{\theta}}_0^2 + \frac{3\mu(\bar{x}_0 - \bar{\rho}_0)(\bar{x}_0 + \bar{\rho}_0)}{(\bar{x}_0^2 + \bar{\rho}_0^2)^{5/2}} + \frac{7\omega^2}{2}\right)^2 > 0 \tag{58}$$

$$(a + d + ef) = -3\dot{\bar{\theta}}_0^2 + \frac{\mu}{(\bar{x}_0^2 + \bar{\rho}_0^2)^{3/2}} + \frac{5\omega^2}{2} \tag{59}$$

With two of these roots always having positive signs, only purely imaginary roots will allow for a stable solution and they depend on the comet's specific orbit. Therefore, to have purely imaginary roots, the following condition needs to hold for the comet's orbit:

$$(a + d + ef) < -\sqrt{4b^2 + (-a + d + ef)^2} \tag{60}$$

because $\sqrt{4b^2 + (-a + d + ef)^2} > 0$ always.

As an example, Fig. 11 illustrates the stable and unstable circular orbit equilibrium solutions based on this analysis. The eigenvalues are indeed either zero or purely imaginary for the stable solutions.

To test this stability criteria, example simulations of stable and unstable solutions as determined by Eq. (60) were performed and their trajectories were plotted on the appropriate zero-velocity curve. Figure 12 shows a stable trajectory remaining close to the equilibrium point. Note that the zero-velocity curves are computed for the averaged equations with a slightly different energy (a result of terms that have been averaged out) than the nonaveraged equations, yielding a curve around the averaged equilibrium solution instead of a single point. Figure 13 shows an unstable trajectory wandering far from the equilibrium point as expected and eventually escaping. These results provide an analytical method of determining stable orbits in the Hill rotating system about a small body under solar radiation pressure.

Until this point, the analysis presented could be applied to any small body without disturbing forces other than solar radiation pressure. Let us shift our focus to a comet with outgassing jets that produce a varied pressure field in the vicinity of the comet nucleus. The acceleration due to an outgassing jet will be considered as a radial force with the acceleration vector defined as follows [4]:

$$\mathbf{a}_{oj} = (A_{\text{og}}/|\mathbf{r}|^3)\mathbf{r} \tag{61}$$

where A_{og} is the strength of the outgassing jet. The new equations of motion become

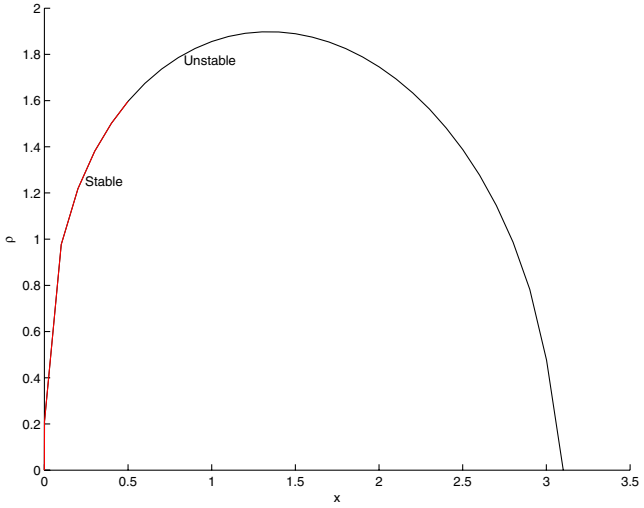

Fig. 11 Possible circular orbit solutions as a function of x from averaged equations.

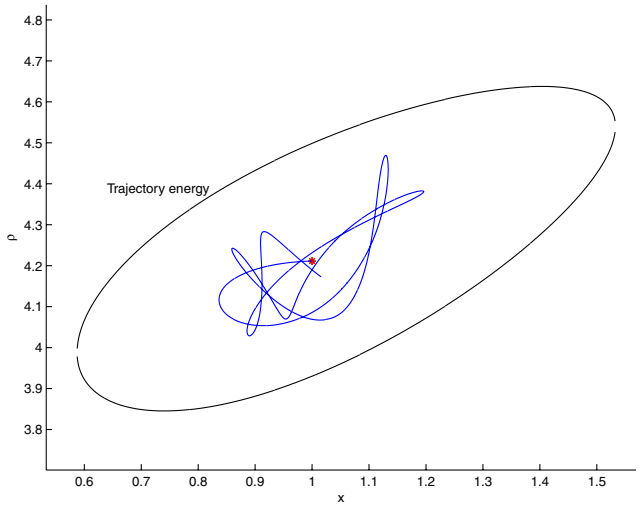

Fig. 12 Stable trajectory plotted with zero-velocity curve showing the trajectory energy and the averaged equilibrium solution energy, where ∗ is the averaged equilibrium solution.

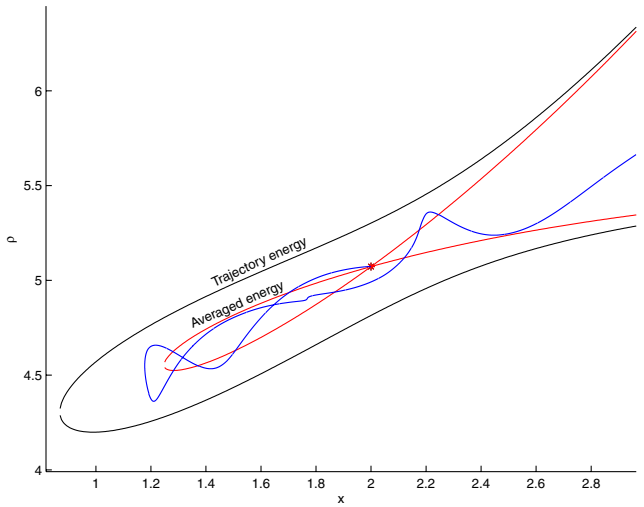

Fig. 13 Unstable trajectory plotted with zero-velocity curve showing the trajectory energy and the averaged equilibrium solution energy, where ∗ is the averaged equilibrium solution.

$$\ddot{\mathbf{r}}_I = \frac{\partial U}{\partial \mathbf{r}_I} + g\hat{d} + \mathbf{a}_{\text{oj}} \tag{62}$$

When broken down into cylindrical coordinates, it becomes obvious that only the x and ρ directions are affected by the outgassing jet's acceleration.

$$\ddot{x} = 2\omega(\dot{\rho}\cos\theta - \rho\dot{\theta}\sin\theta) + 3\omega^2 x + g - (x\mu/r^3) + (xA_{\text{og}}/r^3) \tag{63}$$

$$\ddot{\rho} = -2\dot{x}\omega\cos\theta + \rho\dot{\theta}^2 - \rho\omega^2\sin^2\theta - (\rho\mu/r^3) + (\rho A_{\text{og}}/r^3) \tag{64}$$

$$\rho\ddot{\theta} = 2\dot{x}\omega\sin\theta - 2\dot{\rho}\,\dot{\theta} - \rho\omega^2\sin\theta\cos\theta \tag{65}$$

Therefore, the new Jacobi integral is

$$J_{\text{og}} = \tfrac{1}{2}(\dot{x}^2 + \dot{\rho}^2 + \rho^2\dot{\theta}^2) - (\mu/r) - \tfrac{1}{2}\omega^2(3x^2 - \rho^2\sin(\theta)^2) - gx + (A_{\text{og}}/r) \tag{66}$$

Averaging this over θ as before yields

$$\bar{J}_{\text{og}} = \tfrac{1}{2}(\dot{\bar{x}}^2 + \dot{\bar{\rho}}^2) - (\mu/\bar{r}) - \tfrac{1}{2}\omega^2(3\bar{x}^2 - \tfrac{1}{2}\bar{\rho}^2) - g\bar{x} + (h^2/2\bar{\rho}^2) + (A_{\text{og}}/r) \tag{67}$$

If we consider that the spacecraft passes through an outgassing jet's pressure field, we can determine a bound on the strength of the jet for which the spacecraft is contained within an area about a stable equilibrium solution. As determined previously, the stable equilibrium solution has a conjugate h-valued unstable equilibrium solution that defined the closure point on the zero-velocity curve with increased energy. Define C_s as the energy associated with a stable equilibrium solution with angular momentum magnitude, h, and C_u as the energy associated with the conjugate unstable equilibrium solution. Therefore, the condition $C_s \leq C_{\text{og}} \leq C_u$, where C_{og} is the energy while within an outgassing jet, must hold to keep a spacecraft bounded near the stable equilibrium. This implies a bound on the outgassing magnitude, A_{og}:

$$(A_{\text{og}}/\bar{r}) \leq C_u - C_s \tag{68}$$

or

$$A_{\text{og}} \leq (C_u - C_s)\bar{r} \tag{69}$$

Therefore, if the strength of an outgassing jet, A_{og}, can be estimated, this bound gives insight into whether the spacecraft will remain trapped in the vicinity of the stable equilibrium. For example, Fig. 14 illustrates the trajectory of a spacecraft that has passed though an outgassing jet with a magnitude that does not violate the criteria and allows for the spacecraft to remain bounded near the equilibrium solution. The magnitude of the outgassing jet in Fig. 15 is too large and forces an instability in the orbit, allowing it to escape.

VI. Orbital Control

Because it has been shown that stable orbits exist, we now consider controlling these orbits. Orbits that are restricted to an interval of θ on the comet's terminator would be useful for monitoring the comet's surface at sunrise or sunset, where interesting surface activity occurs. Several control schemes are presented to restrict the motion of an orbiting spacecraft using a single- or two-dimensional surface to define the boundary of the allowable orbit. Different control boundaries will be considered when developing a control scheme. In the first case, the motion is restricted by an angle in the cylindrical coordinate formulation of the equations of motion. This produces a long wedge-shaped allowable area with the possibility of impact with the nucleus. In the second case, boundaries defined by both an angle and a

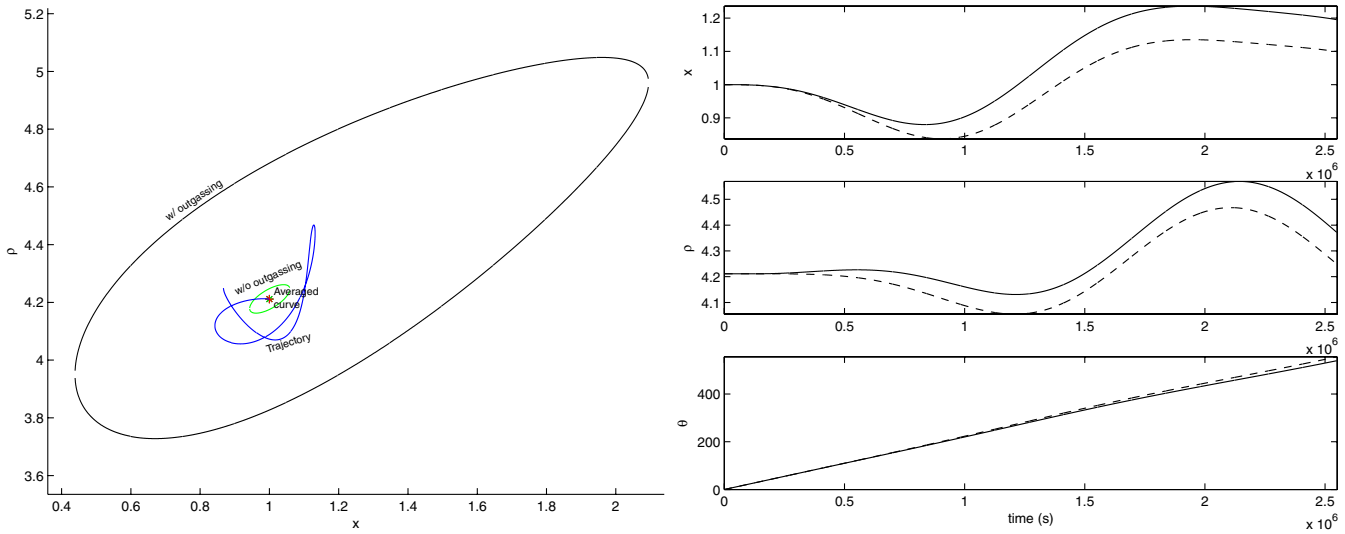

Fig. 14 Shown are the following: a) stable trajectory in the presence of an outgassing jet on appropriate zero-velocity curve showing the zero-velocity curve with and without outgassing, the zero-velocity curve without outgassing, the average equilibrium solution zero-velocity curve, the trajectory; and b) solid line: the trajectory with outgassing shown with position components, and b) dashed line: the trajectory without outgassing.

minimum radius that also restrict impacting are tested. In each case, an acceleration is applied when the spacecraft violates the defined boundary to push the spacecraft back into the allowable motion area [5].

For our initial analysis, we consider a theoretical control method that is commonly used to test the feasibility of the control boundaries, an impulsive thrust. First consider the case in which a Δv is applied to reverse the direction of the full velocity vector while holding the magnitude constant. This result, as seen in Fig. 16, does not maintain the orbit perpendicular to the sun line, evidenced by the drift in x in Fig. 16, although the impulsive maneuver is successful at not violating the boundaries.

Because the reversal of the full velocity vector performs poorly at maintaining the orbit's attitude, we consider the same impulse maneuver except that we only reverse the $\dot{y}$ and $\dot{z}$ components (or the $\dot{\rho}$ and $\dot{\theta}$ components). We also consider an impulse maneuver that only reverses the $\dot{\theta}$ component.

Figure 17 shows a comparison of the three impulsive schemes for the angle boundary. It is clear that the reversal of the $\dot{\rho}$ and $\dot{\theta}$ velocity components is the best of the three at maintaining the orbit across all three position components.

The drawback to the boundary defined by angles is that the spacecraft can be contained within the bounded area and still impact the comet. We now consider an orbit bounded by the angles as before and also a minimum radius from the body. When the spacecraft encounters the angle boundary, a reversal of the $\dot{\theta}$ velocity component impulse will be applied, whereas a reversal of the $\dot{\rho}$ velocity component impulse will be applied when the radius boundary is violated. We note that both methods give similar results and thus do not show the $\dot{\rho}$ velocity reversal in our plots.

The control schemes up until this point have been impulsive thrust maneuvers with the main objective of confining the spacecraft within a region. These methods were necessary to illustrate that the spacecraft could be controlled to remain within an allowable region and not escape. We now consider a finite burn based on the best impulsive control with the following form:

$$\mathbf{a} = m[0, -v_{\dot{\rho}}, -v_{\dot{\theta}}] \tag{70}$$

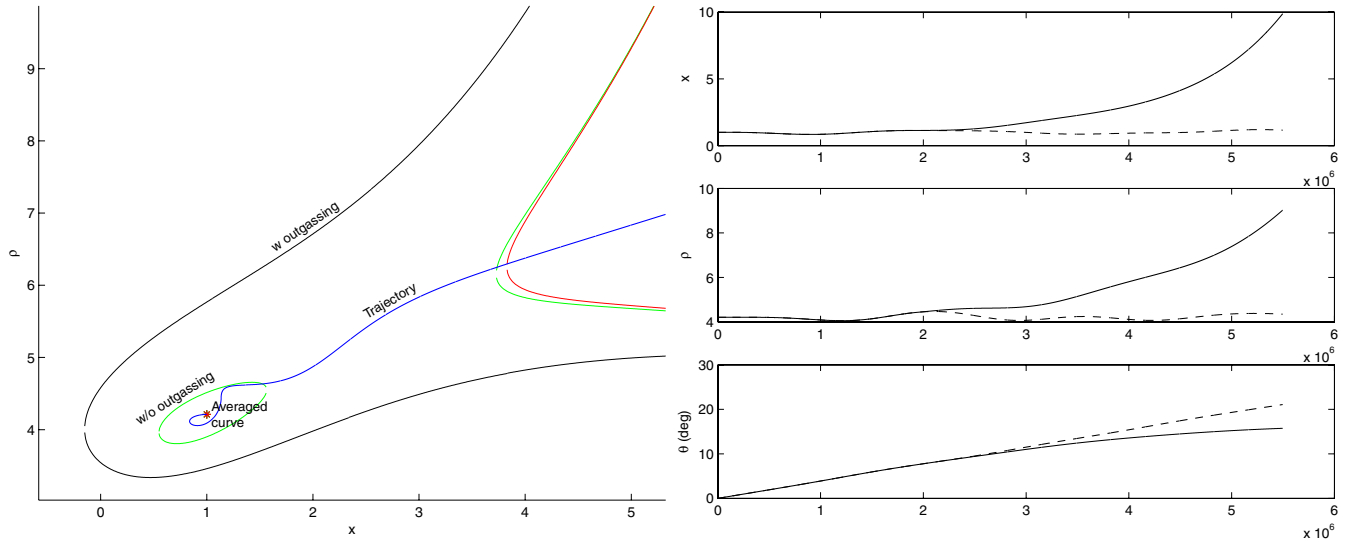

Fig. 15 Shown are the following: a) unstable trajectory in the presence of an outgassing jet on appropriate zero-velocity curve showing the zero-velocity curve with and without outgassing, the zero-velocity curve without outgassing, the average equilibrium solution zero-velocity curve, the trajectory; and b) solid line: the trajectory with outgassing shown with position components, and b) dashed line: the trajectory without outgassing.

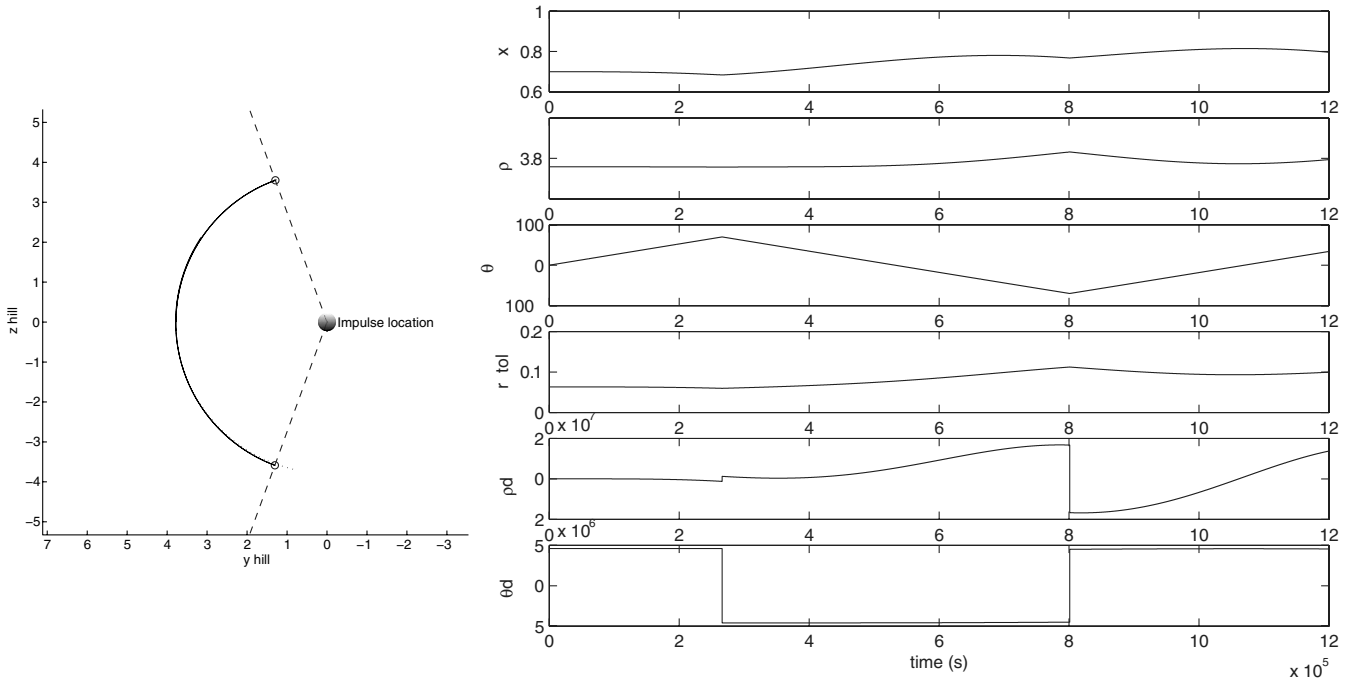

Fig. 16 Shown are the following: a) orbit control with full reversed velocity impulse with angle boundary (solid line: controlled trajectory, dashed line: angle boundary), and b) position and velocity components of the controlled orbit, plotted for reference.

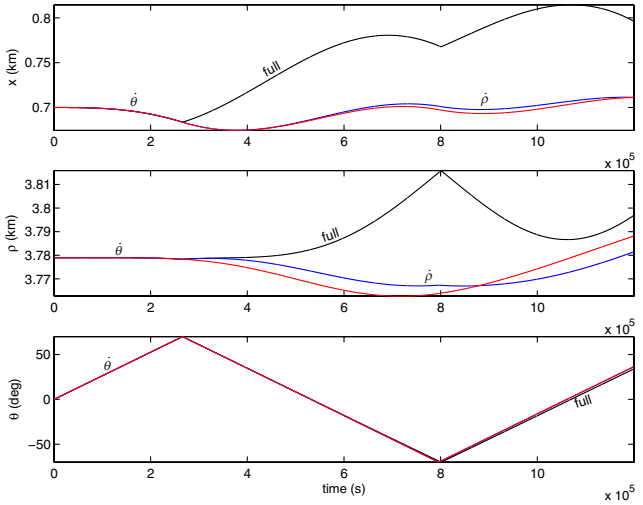

Fig. 17 Orbit control comparison with angle boundary showing the full velocity reversal, $\dot{\rho}$, and $\dot{\theta}$ reversal, and $\dot{\theta}$ reversal.

where m is a scale factor and $-v_{\dot{\rho}}$ and $-v_{\dot{\theta}}$ are the velocity components of the spacecraft at the time of boundary crossing. Note that this control thrust has a constant magnitude and direction. The thrust is turned on when the spacecraft crosses the boundary angle and turned off once its $\dot{\theta}$ becomes the negative of the value at the boundary crossing. Figures 18 and 19 illustrate the finite burn control for a range of angle boundaries. Note that the deviation from the initial circular orbit depends on the x offset and the scale factor, m. These represent a more realistic case of orbit control, although we note that other important effects such as orbit uncertainty and central body nonsphericity have not been incorporated. These effects will be studied in a future work.

VII. Conclusions

We have shown that, on average, sun-synchronous circular orbits offset from the center of mass of the body exist in the Hill equations of motion with solar radiation pressure. The construction of the zero-velocity curves provide insight into the stability of these orbits and allows one to evaluate stability in the presence of pressure

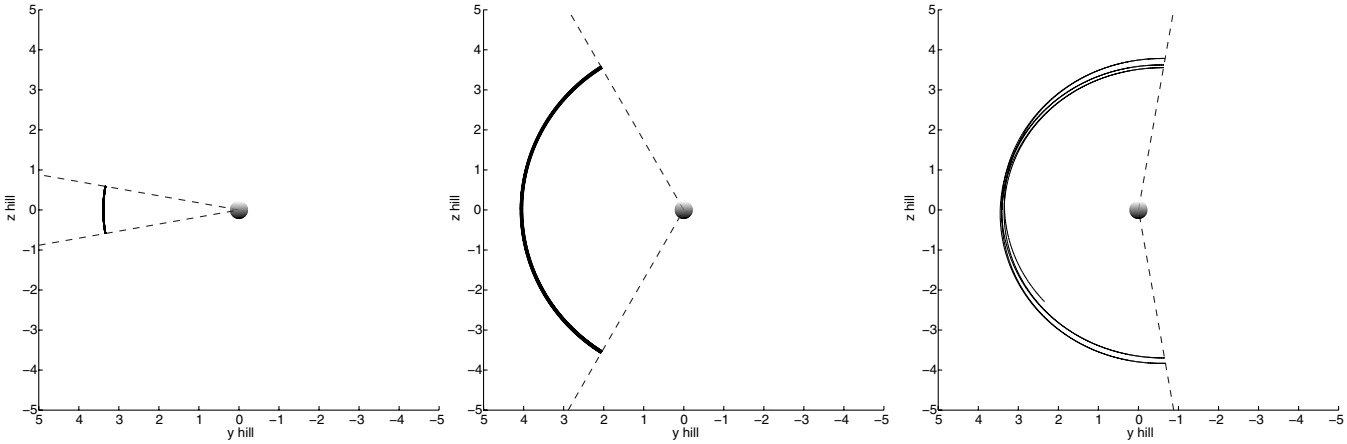

Fig. 18 Orbit with initial offset of $x = 1$ km with angle boundary at ± 10, ± 50, and ± 110 deg. Solid line: controlled trajectory with finite burn reversal of $\dot{\rho}$ and $\dot{\theta}$ velocity components, dashed line: angle boundary.

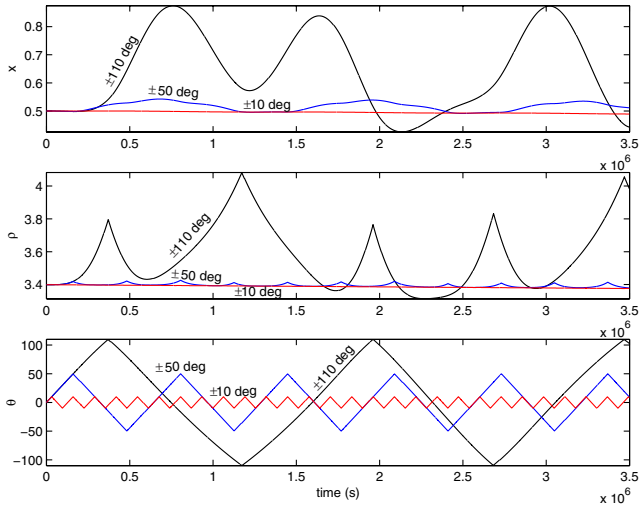

Fig. 19 Orbit control comparison with varied angle boundary.

from an outgassing jet. The stability of the orbits deemed stable by zero-velocity curve analysis was verified though spectral stability analysis. Criteria was given to produce stable orbits for a given system in the vicinity of cometary outgassing jets. Multiple control schemes were presented to restrict the motion of the spacecraft within a defined bounded area.

Acknowledgments

We acknowledge support for this research from the Jet Propulsion Laboratory Interplanetary Network Directorate Technology Program and comments from Shyam Bhaskaran at the Jet Propulsion Laboratory.

References

[1] Dankowicz, H., "Some Special Orbits in the Two-Body Problem with Radiation Pressure," *Celestial Mechanics and Dynamical Astronomy*, Vol. 58, 1994, pp. 353–370.doi:10.1007/BF00692010

[2] Scheeres, D. J., and Marzari, F., "Spacecraft Dynamics in the Vicinity of a Comet," *Journal of the Astronautical Sciences*, Vol. 50, No. 1, 2002, pp. 35–52.

[3] Scheeres, D. J., "Satellite Dynamics About Small Bodies: Averaged Solar Radiation Pressure Effects," *Journal of the Astronautical Sciences*, Vol. 47, No. 1, 1999, pp. 25–46.

[4] Byram, S. M., and Scheeres, D. J., "Models for the Comet Dynamical Environment," *Journal of Guidance, Control, and Dynamics*, Vol. 30, No. 5, 2007, pp. 1445–1454.
doi:10.2514/1.28299

[5] Broschart, S. B., and Scheeres, D. J., "Boundedness of Spacecraft Hovering Under Dead-Band Control in Time-Invariant Systems," *Journal of Guidance, Control, and Dynamics*, Vol. 30, No. 2, 2007, pp. 601–610.
doi:10.2514/1.20179

[6] Villac, B. F., and Scheeres, D. J., "Escape Trajectories in the Hill Three-Body Problem and Applications," *Journal of Guidance, Control, and Dynamics*, Vol. 26, No. 2, 2003, pp. 224–232.
doi:10.2514/2.5062